Supplement of Atmos. Meas. Tech., 18, 695–716, 2025
https://doi.org/10.5194/amt-18-695-2025-supplement

Atmospheric Measurement Techniques
Open Access
EGU

Supplement of

Global decadal measurements of methanol, ethene, ethyne, and HCN from the Cross-track Infrared Sounder

Kelley C. Wells et al.

Correspondence to: Dylan B. Millet (dbm@umn.edu)

S1 CrIS spectral residual analysis

The CrIS spectral residuals used here and plotted in Fig. 2e were processed with the MUlti-SpEctra, MUltiSpEcies, Multi-SEnsors (MUSES) algorithm from the TRopospheric Ozone and its Precursors from Earth System Sounding (TROPESS) project. The MUSES algorithm leverages over 20 years of heritage from the Aura TES optimal estimation algorithm. The residual strategy employed here differs from that of the standard TROPESS CrIS processing: standard processing aims to estimate the optimal abundance for relevant absorbers, whereas the goal for this work is to remove non-target absorber signals. Following the standard initial guess refinement for clouds and surface temperature (Bowman et al., 2021), a joint retrieval for H_2O, CO_2, O_3, NH_3, PAN, HDO, N_2O, CH_4, cloud properties, surface temperature, and atmospheric temperature is performed. The radiative transfer also accounts for fixed climatological SO_2, HNO_3, OCS, SF_6, HCOOH, CFC-11, CFC-12, and CCl_4 profiles. Spectral windows span 650 to 1750 cm^{-1}, with gaps where radiances do not fit well (e.g., due to spectroscopic uncertainties). Following the joint step, cloud properties, surface properties, and atmospheric temperature are fixed, and PAN is retrieved between 780 and 790 cm^{-1} (with a 783.125-786.250 cm^{-1} gap to window around water interferences). Next, ozone and ammonia are updated using windows between 923.125 and 1317.5 cm^{-1}. Finally, the spectral residual is calculated for the full CrIS LWIR band (650-1095 cm^{-1}), accounting for H_2O, HDO, CO_2, O_3, N_2O, CH_4, SO_2, NH_3, HNO_3, OCS, SF_6, HCOOH, PAN, CFC-11, CFC-12, and CCl_4.

S2 GEOS-Chem CTM

We use the GEOS-Chem 3D chemical transport model (CTM) to generate the VOC profiles used as ANN input in the ROCRv2 retrievals, and to interpret the resulting CrIS observations. The model (13.2.2; https://doi.org/10.5281/zenodo.5711194) employs MERRA-2 meteorological data from the NASA Global Modeling and Assimilation Office (GMAO), here regridded to 2° latitude × 2.5° longitude with 47 levels from the surface to 0.01 hPa. Simulations use a 10-min transport timestep (20-min for emissions and chemistry) and one-year initialization. Model output for 1200-1500 LT, corresponding to the approximate range in daytime CrIS overpass times, is used to train the ANN.

GEOS-Chem includes detailed HO_x-NO_x-VOC-ozone-BrO_x chemistry coupled to aerosols (Millet et al., 2015; Mao et al., 2013). The version employed here includes simplified ethyne and ethene chemistry that accounts for their reactions with ozone and OH (Kwon et al., 2021). It also incorporates recent updates for methanol, in particular for its secondary production via reactions of methylperoxy radicals with OH and other methylperoxy radicals (Bates et al., 2021). HCN is not a standard GEOS-Chem tracer and was added here following a previously-developed offline simulation (Li et al., 2003; Li et al., 2009). Biogenic emissions of VOCs are simulated using a grid-independent implementation of MEGANv2.1 (Guenther et al., 2012), while anthropogenic emissions are based on the Community Emissions Data System (CEDS) inventory (Mcduffie et al., 2020). The Global Fire Emissions Database v4 (GFEDv4; (Van Der Werf et al., 2017) is used to compute biomass burning emissions, and

we also employ the Global Fire Assimilation System (GFAS; (Di Giuseppe et al., 2018) in a sensitivity analysis to test how differing vertical mixing assumptions impact the CrIS retrievals. Whereas fire emissions in GFEDv4 are emitted at the surface, GFAS as implemented in GEOS-Chem distributes its emissions uniformly between the surface and the 'mean altitude of maximum injection', which is computed locally using a plume rise model and MODIS Fire Radiative Power (FRP) observations (Jin et al., 2023; Freitas et al., 2007; Latham, 1994).

Species	Site	r (daily, monthly)	Offset (daily, monthly)
Methanol	Maido	0.61, 0.63	3.7×10^{15}, 3.7×10^{15}
	Porto Velho	0.94, 0.99	1.1×10^{16}, 8.4×10^{15}
	Saint Petersburg	0.69, 0.68	1.1×10^{16}, 5.3×10^{15}
	Toronto	0.64, 0.76	1.9×10^{16}, 1.3×10^{16}
	Jungfraujoch	0.53, 0.31	3.4×10^{15}, 2.1×10^{15}
Ethyne	Toronto	0.48, 0.43	2.0×10^{15}, 1.9×10^{15}
	Jungfraujoch	0.59, 0.69	6.6×10^{14}, 4.8×10^{14}
	Wollongong	0.31, 0.48	4.5×10^{14}, -3.3×10^{12}
	Xianghe	0.55, 0.57	2.6×10^{15}, 2.4×10^{15}
	Boulder	0.59, 0.66	1.0×10^{15}, 6.8×10^{14}
	Porto Velho	0.57, 0.85	7.2×10^{14}, 6.5×10^{14}
	Maido	0.51, 0.68	2.7×10^{14}, 2.3×10^{14}
HCN	Maido	0.46, 0.49	2.7×10^{15}, 2.7×10^{15}
	Porto Velho	0.66, 0.87	4.1×10^{15}, 3.3×10^{15}
	Saint Petersburg	0.15, -0.15	4.2×10^{15}, 7.6×10^{15}
	Toronto	0.48, 0.14	4.1×10^{15}, 3.7×10^{15}
	Jungfraujoch	0.47, 0.42	3.7×10^{15}, 3.5×10^{15}
	Wollongong	0.48, 0.64	3.2×10^{15}, 2.4×10^{15}
	Xianghe	-0.36, -0.55	7.1×10^{15}, 7.3×10^{15}
	Boulder	-0.14, -0.38	5.6×10^{15}, 5.4×10^{15}
	Bremen	0.19, 0.06	3.5×10^{15}, 3.2×10^{15}
	Mauna Loa	0.58, 0.67	3.6×10^{15}, 3.6×10^{15}
	Lauder	0.52, 0.70	2.7×10^{15}, 2.2×10^{15}
	Paramaribo	0.57, 0.56	5.7×10^{15}, 5.9×10^{15}
	Rikubetsu	0.02, 0.00	3.5×10^{15}, 3.1×10^{15}
	St. Denis	0.70, 0.74	2.7×10^{15}, 2.6×10^{15}
	Izaña	0.35, 0.44	3.6×10^{15}, 3.4×10^{15}
	Zugspitze	0.36, 0.38	2.8×10^{15}, 2.4×10^{15}

Table S1. CrIS:NDACC comparisons statistics by site. Correlation coefficients and offsets (molec/cm^2) are listed for both daily and monthly means.

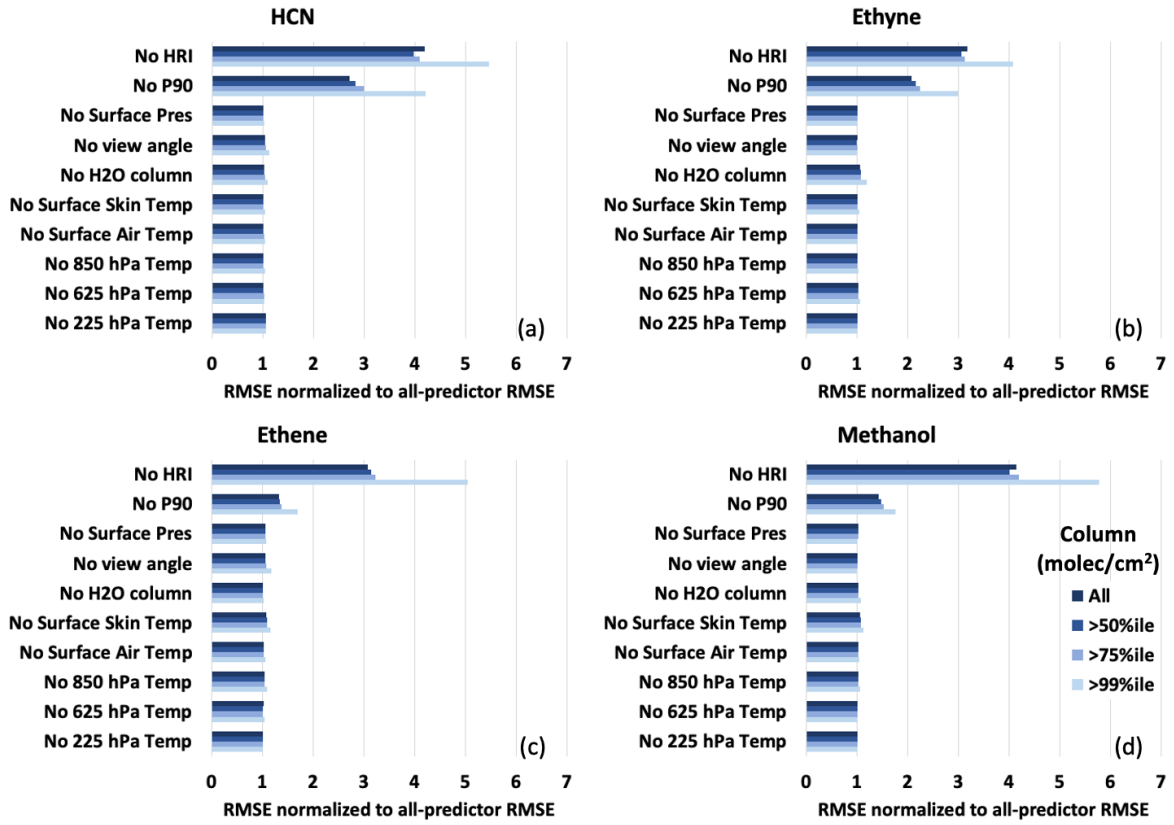

40 **Figure S1. ANN predictor importance as a function of column abundance. Shown is the normalized root mean squared error (RMSE) for tests with each variable independently withheld. Data are normalized to the all-predictor RMSE in each case and plotted for different column abundance percentile bins.**

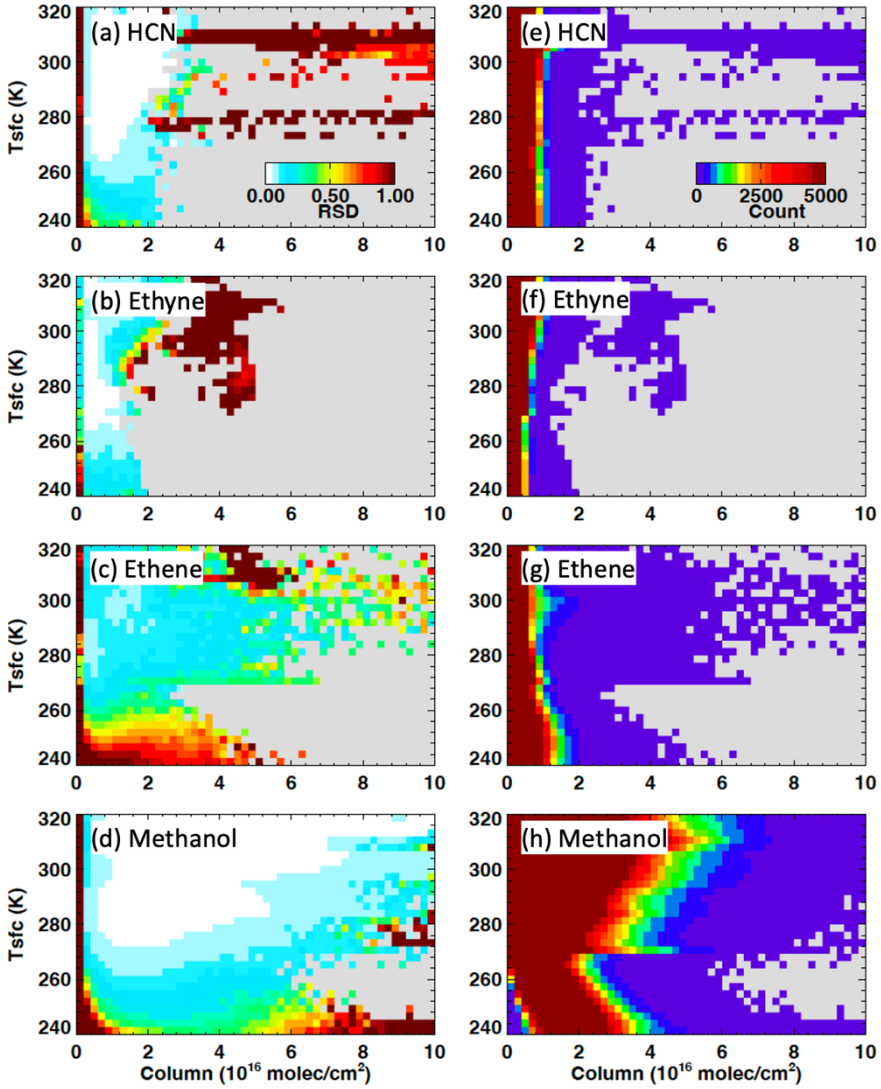

Figure S2. ROCRv2 prediction precision as a function of column amount and thermal contrast. Data plotted reflect the relative standard deviation of the 10-ANN predictions for each CrIS retrieval (left column) or the number of observations in each bin (right column) binned by surface temperature and column amount.

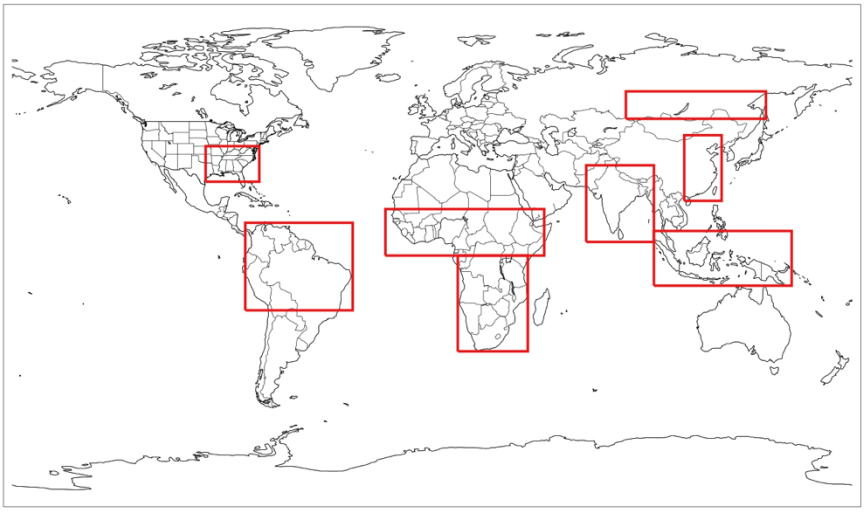

Figure S3. Region boundaries used for analyses described in the main text.

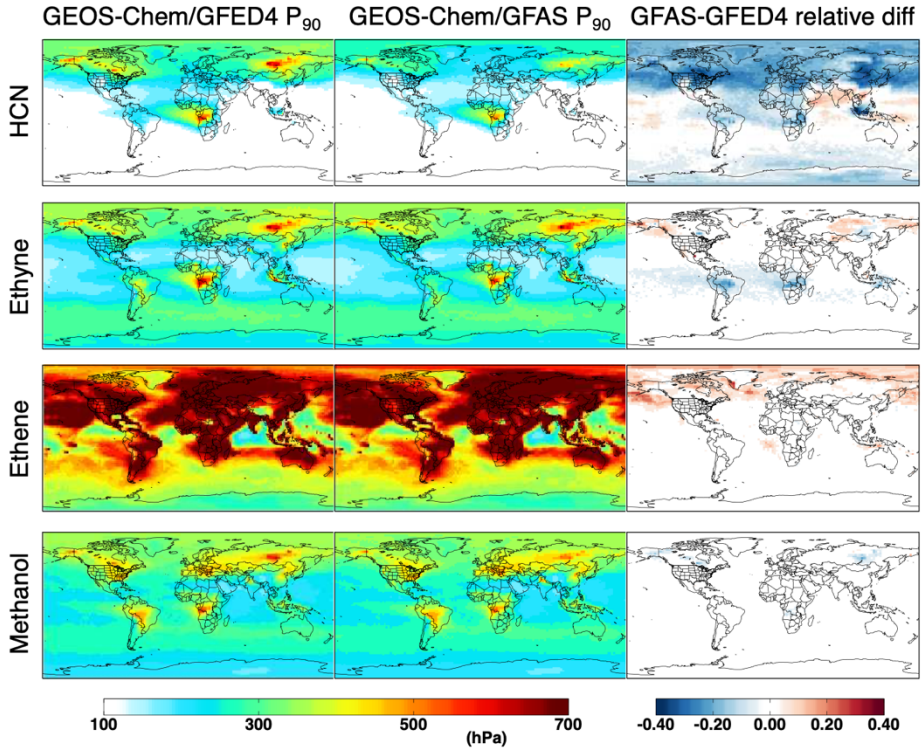

Figure S4. P_{90} values as predicted by GEOS-Chem during July 2019 for a base-case simulation employing GFEDv4 biomass burning emissions (left column) and for a sensitivity run using GFAS biomass burning emissions (middle column). Right column shows the relative difference between the two (GFAS-GFEDv4 P_{90}).

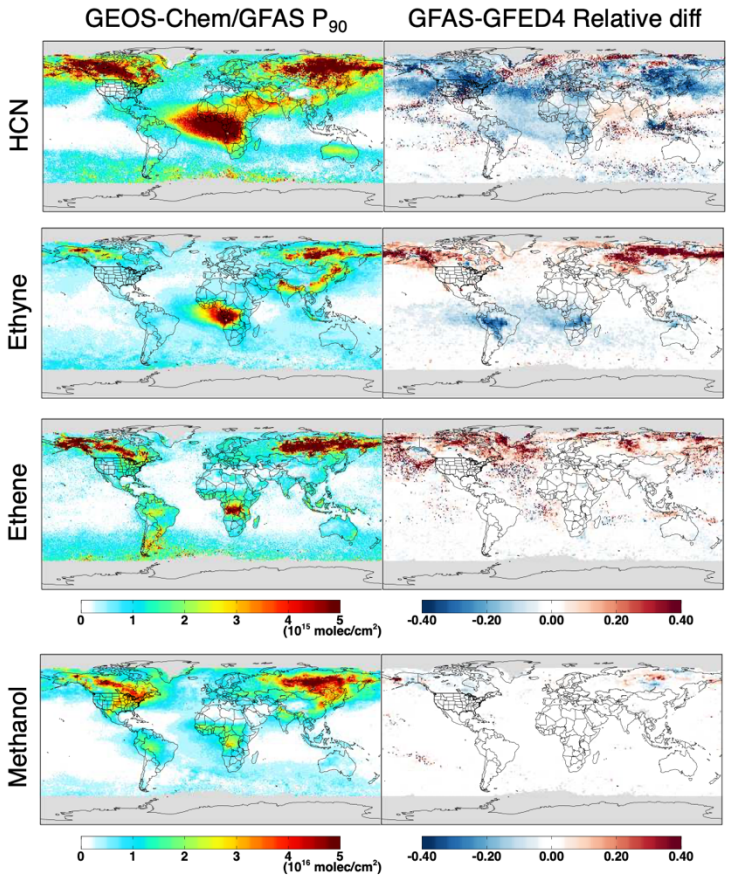

55 **Figure S5. Accounting for vertical profile uncertainty in the CrIS VOC retrievals. Plotted are CrIS-retrieved column enhancements as derived for July 2019 when using P_{90} fields predicted using a GEOS-Chem simulation with GFAS biomass burning emissions (left column), and their relative difference with respect to results obtained using GFEDv4 biomass burning emissions (right column).**

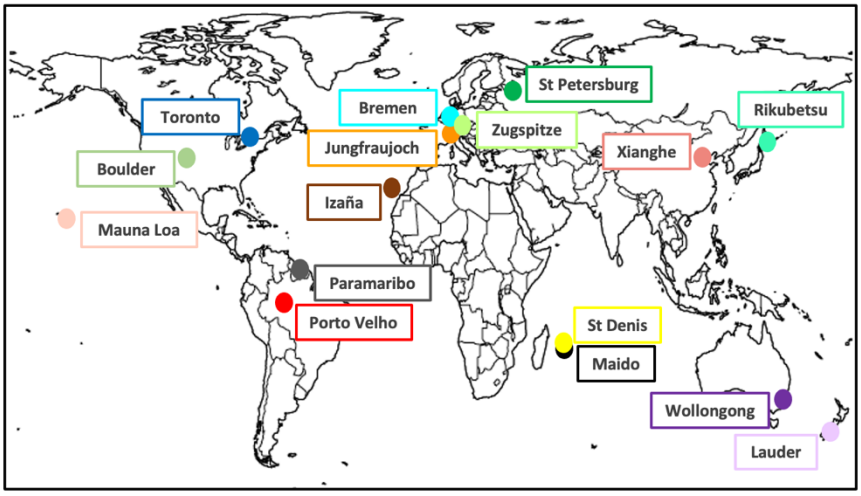

Figure S6. Locations of the ground-based FTIR sites used to evaluate the CrIS VOC retrievals. All sites are part of the NDACC network aside from Porto Velho, Brazil and Xianghe, China which are currently NDACC candidate sites.

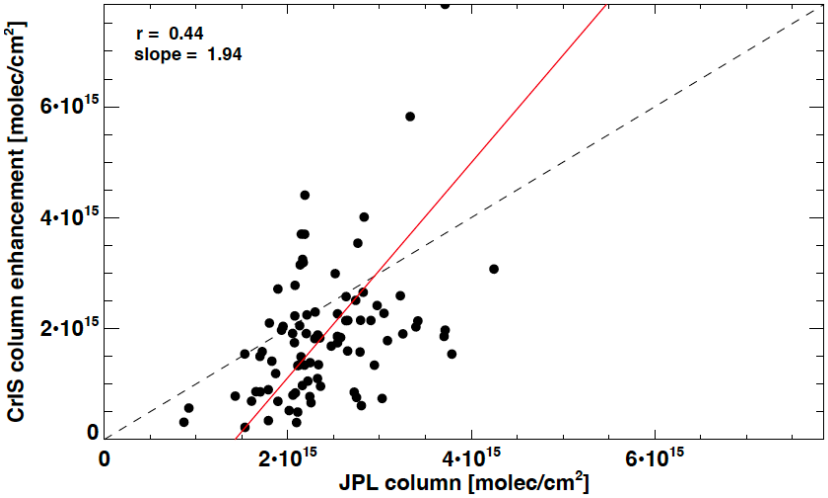

Figure S7. Evaluation of CrIS ethene against the MkIV interferometer at JPL in Pasadena. Data represent monthly means that have been adjusted to the GEOS-Chem predicted P_{90}.

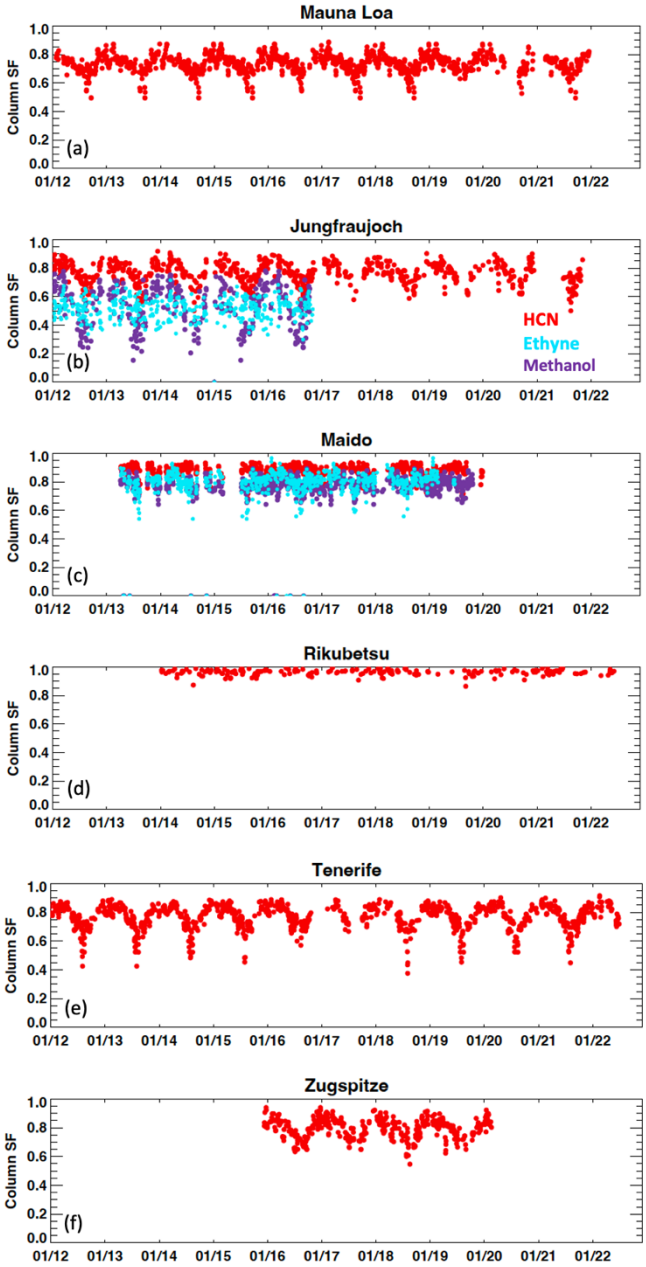

Figure S8. VOC column adjustments used to account for elevation differences between high-altitude NDACC station and the surrounding CrIS pixels. Data plotted represent scaling factors calculated as the above-site fraction of the total column based on local GEOS-Chem predictions for HCN (red), ethyne (cyan), and methanol (purple).

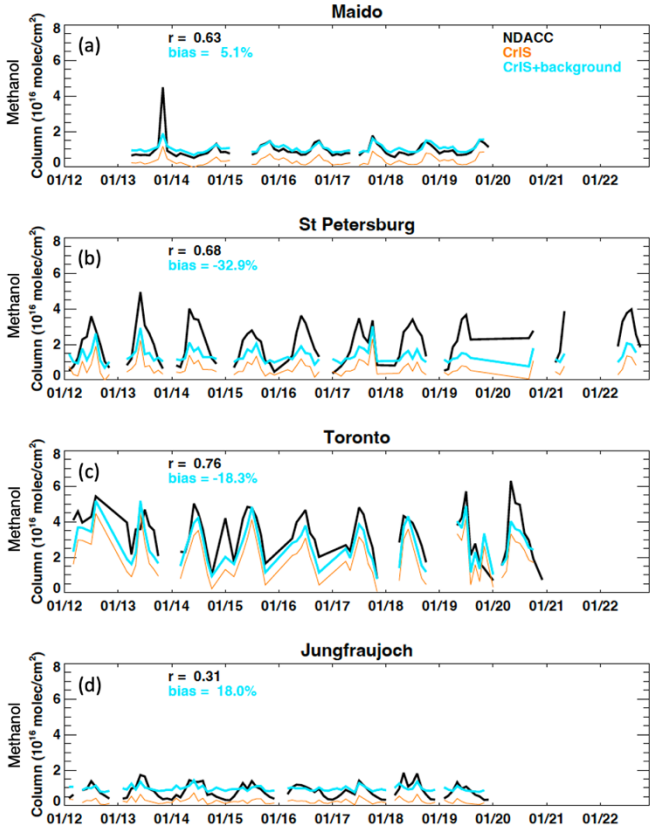

Fig S9. Timeseries comparison of CrIS and NDACC methanol observations. Plotted are the NDACC monthly mean total columns (black), the CrIS column enhancements (orange), and the CrIS column enhancements plus background (cyan). CrIS observations are averaged over the 3×3 pixel area encompassing the site to increase data coverage. Correlation coefficients and normalized mean biases (NMB) are computed after background correction and for the CrIS pixel directly overlying the NDACC station. Porto Velho is omitted from this figure due to the short duration of that data record.

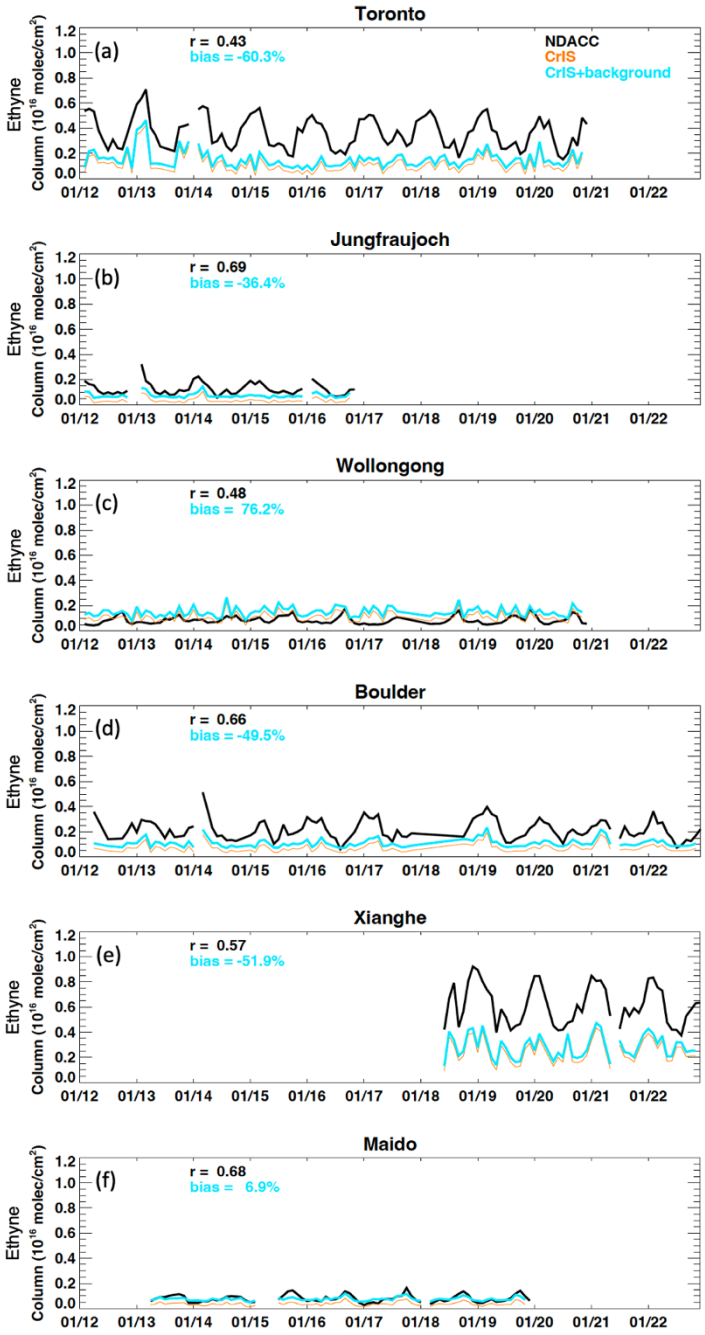

Fig S10. Timeseries comparison of CrIS and NDACC ethyne observations. Plotted are the NDACC monthly mean total columns (black), the CrIS column enhancements (orange), and the CrIS column enhancements plus background (cyan). CrIS observations are averaged over the 3×3 pixel area encompassing the site to increase data coverage. Correlation coefficients and normalized mean biases (NMB) are computed after background correction and for the CrIS pixel directly overlying the NDACC station. Porto Velho is omitted from this figure due to the short duration of that data record.

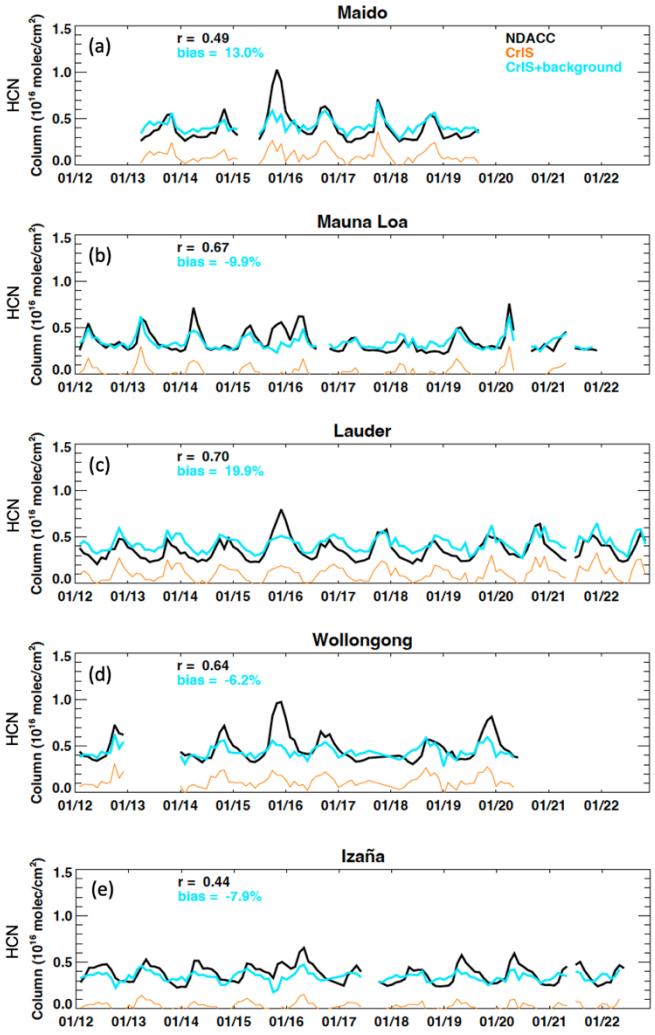

Fig S11. Timeseries comparison of CrIS and NDACC HCN observations at tropical and Southern Hemisphere sites. Plotted are the NDACC monthly mean total columns (black), the CrIS column enhancements (orange), and the CrIS column enhancements plus background (cyan). CrIS observations are averaged over the 3×3 pixel area encompassing the site to increase data coverage. Correlation coefficients and normalized mean biases (NMB) are computed after background correction and for the CrIS pixel directly overlying the NDACC station. St. Denis, Paramaribo, and Porto Velho are omitted from this figure due to the short duration and/or intermittence of those data records.

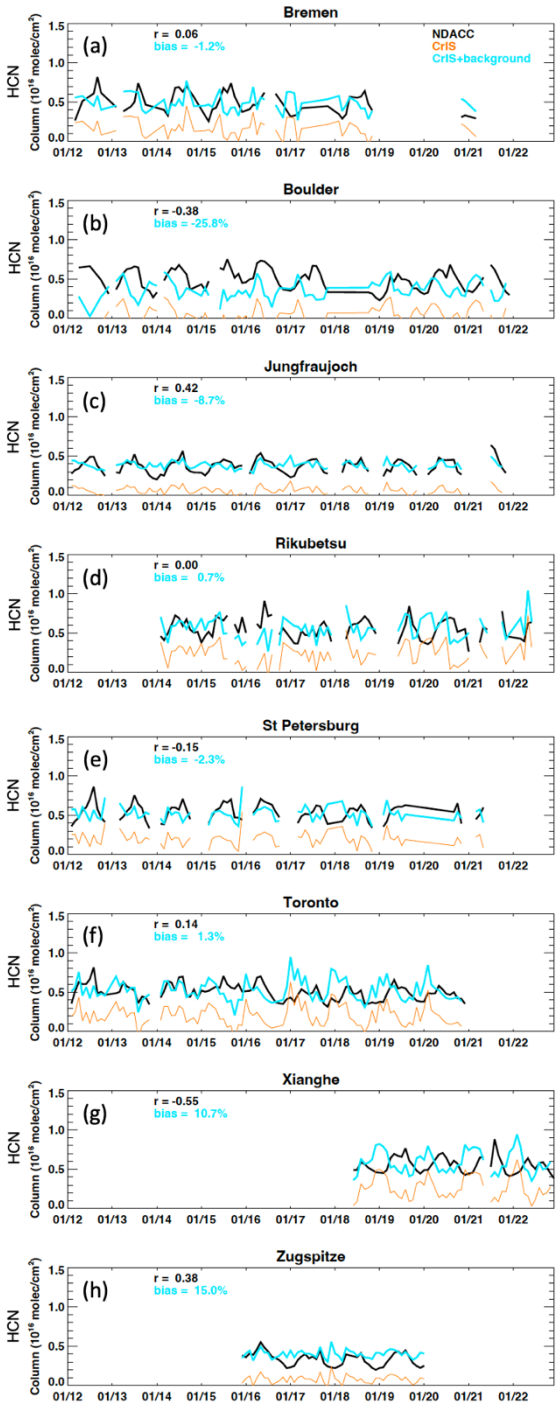

Fig S12. Timeseries comparison of CrIS and NDACC HCN observations at Northern Hemisphere extratropical sites. Plotted are the NDACC monthly mean total columns (black), the CrIS column enhancements (orange), and the CrIS column enhancements plus background (cyan). CrIS observations are averaged over the 3×3 pixel area encompassing the site to increase data coverage.

Correlation coefficients and normalized mean biases (NMB) are computed after background correction and for the CrIS pixel directly overlying the NDACC station.

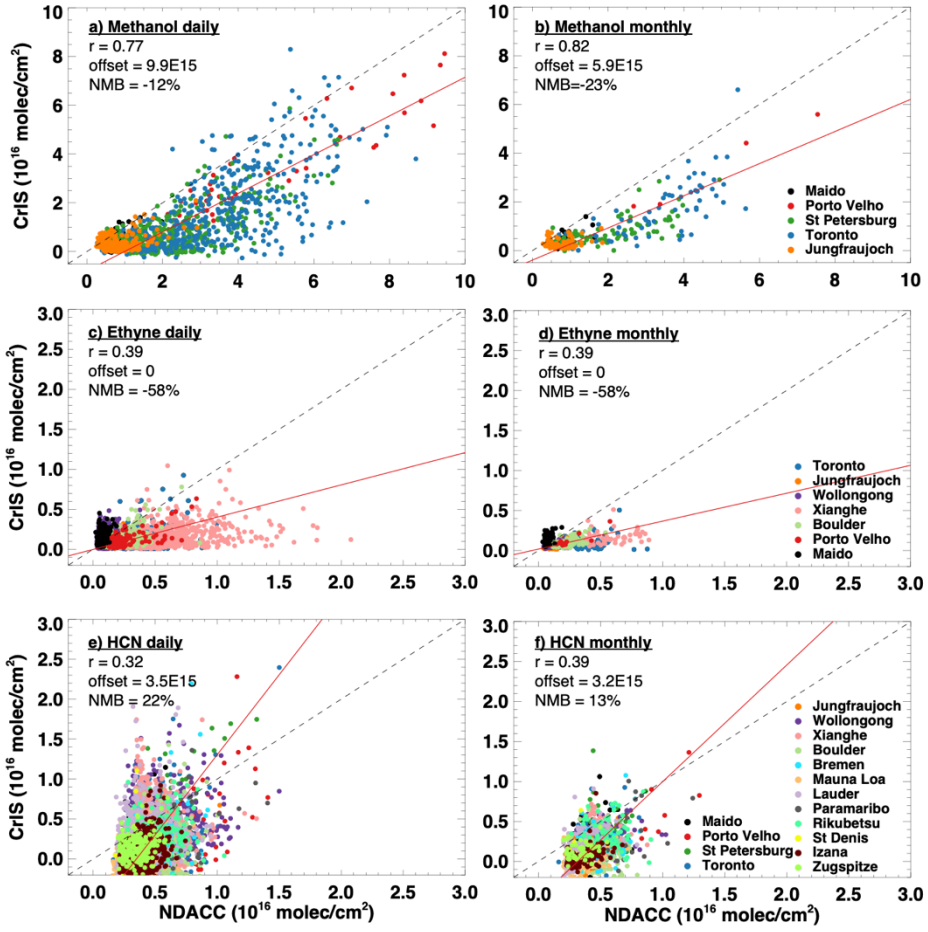

Figure S13. Evaluation of the CrIS VOC retrievals against NDACC ground-based FTIR measurements when applying alternative vertical profile constraints. Plot is the same as Figure 11 except that the CrIS retrievals have been interpolated to the P_{90} values predicted by GEOS-Chem for each location and time rather than to the NDACC-retrieved values.

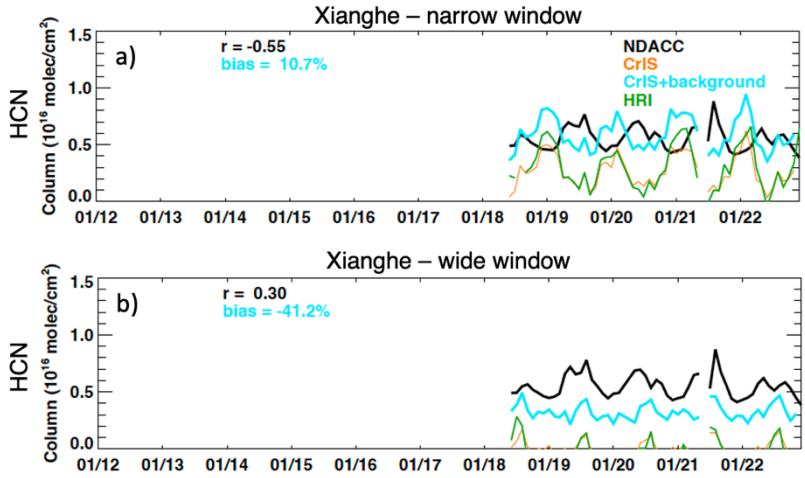

Fig S14. Impact of a) narrow versus b) wide spectral window selection on HCN retrievals at Xianghe, China. Plotted are the NDACC monthly mean total columns (black), the CrIS column enhancements (orange), the CrIS column enhancements plus background (cyan), and the CrIS HCN HRI (green). CrIS observations are averaged over the 3×3 pixel area encompassing the site to increase data coverage. Correlation coefficients and normalized mean biases (NMB) are computed after background correction and for the CrIS pixel directly over the NDACC station.

SI References

Bates, K. H., Jacob, D. J., Wang, S. Y., Hornbrook, R. S., Apel, E. C., Kim, M. J., Millet, D. B., Wells, K. C., Chen, X., Brewer, J. F., Ray, E. A., Commane, R., Diskin, G. S., and Wofsy, S. C.: The Global Budget of Atmospheric Methanol: New Constraints on Secondary, Oceanic, and Terrestrial Sources, J. Geophys. Res.-Atmos., 126, https://doi.org/10.1029/2020jd033439, 2021.

Bowman, K. W., Worden, J. R., Herman, R., Cady-Pereira, K., Natraj, V., Payne, V. H., Worden, H. M., and Kulawik, S. S.: TROPESS Level 2 Algorithm Theoretical Basis Document (ATBD) V1, at: https://docserver.gesdisc.eosdis.nasa.gov/public/project/TROPESS/TROPESS-ATBDv1.1.pdf, 2021, last access: 5 April 2024.

Di Giuseppe, F., Rémy, S., Pappenberger, F., and Wetterhall, F.: Using the Fire Weather Index (FWI) to improve the estimation of fire emissions from fire radiative power (FRP) observations, Atmos. Chem. Phys., 18, 5359-5370, https://doi.org/10.5194/acp-18-5359-2018, 2018.

Freitas, S. R., Longo, K. M., Chatfield, R., Latham, D., Dias, M., Andreae, M. O., Prins, E., Santos, J. C., Gielow, R., and Carvalho, J. A.: Including the sub-grid scale plume rise of vegetation fires in low resolution atmospheric transport models, Atmos. Chem. Phys., 7, 3385-3398, https://doi.org/10.5194/acp-7-3385-2007, 2007.

Guenther, A. B., Jiang, X., Heald, C. L., Sakulyanontvittaya, T., Duhl, T., Emmons, L. K., and Wang, X.: The Model of Emissions of Gases and Aerosols from Nature version 2.1 (MEGAN2.1): an extended and updated framework for modeling biogenic emissions, Geosci. Model Dev., 5, 1471-1492, https://doi.org/10.5194/gmd-5-1471-2012, 2012.

Jin, L. X., Permar, W., Selimovic, V., Ketcherside, D., Yokelson, R. J., Hornbrook, R. S., Apel, E. C., Ku, I. T., Collett, J. L. C., Sullivan, A. P., Jaffe, D. A., Pierce, J. R., Fried, A., Coggon, M. M., Gkatzelis, G. I., Warneke, C., Fischer, E. V., and Hu, L.: Constraining emissions of volatile organic compounds from western US wildfires with WE-CAN and FIREX-AQ airborne observations, Atmos. Chem. Phys., 23, 5969-5991, https://doi.org/10.5194/acp-23-5969-2023, 2023.

Kwon, H. A., Park, R. J., Oak, Y. J., Nowlan, C. R., Janz, S. J., Kowalewski, M. G., Fried, A., Walega, J., Bates, K. H., Choi, J., Blake, D. R., Wisthaler, A., and Woo, J. H.: Top-down estimates of anthropogenic VOC emissions in South Korea using formaldehyde vertical column densities from aircraft during the KORUS-AQ campaign, Elem. Sci. Anth., 9, https://doi.org/10.1525/elementa.2021.00109, 2021.

Latham, D. J.: PLUMP: a plume predictor and cloud model for fire managers, General Technical Report INT-GTR-314. USDA Forest Service, Intermountain Research Station, Ogden, UT, 15p., 1994.

Li, Q., Palmer, P. I., Pumphrey, H. C., Bernath, P., and Mahieu, E.: What drives the observed variability of HCN in the troposphere and lower stratosphere?, Atmo. Chem. Phys., 9, 8531-8543, https://doi.org/10.5194/acp-9-8531-2009, 2009.

Li, Q. B., Jacob, D. J., Yantosca, R. M., Heald, C. L., Singh, H. B., Koike, M., Zhao, Y. J., Sachse, G. W., and Streets, D. G.: A global three-dimensional model analysis of the atmospheric budgets of HCN and CH3CN: Constraints from aircraft and ground measurements, J. Geophy. Res.-Atmos., 108, https://doi.org/10.1029/2002jd003075, 2003.

Mao, J. Q., Paulot, F., Jacob, D. J., Cohen, R. C., Crounse, J. D., Wennberg, P. O., Keller, C. A., Hudman, R. C., Barkley, M. P., and Horowitz, L. W.: Ozone and organic nitrates over the eastern United States: Sensitivity to isoprene chemistry, J. Geophys. Res.-Atmos., 118, 11256-11268, https://doi.org/10.1002/jgrd.50817, 2013.

McDuffie, E. E., Smith, S. J., O'Rourke, P., Tibrewal, K., Venkataraman, C., Marais, E. A., Zheng, B., Crippa, M., Brauer, M., and Martin, R. V.: A global anthropogenic emission inventory of atmospheric pollutants from sector- and fuel-specific sources (1970-2017): an application of the Community Emissions Data System (CEDS), Earth Syst. Sci. Data, 12, 3413-3442, https://doi.org/10.5194/essd-12-3413-2020, 2020.

Millet, D. B., Baasandorj, M., Farmer, D. K., Thornton, J. A., Baumann, K., Brophy, P., Chaliyakunnel, S., de Gouw, J. A., Graus, M., Hu, L., Koss, A., Lee, B. H., Lopez-Hilfiker, F. D., Neuman, J. A., Paulot, F., Peischl, J., Pollack, I. B., Ryerson, T. B., Warneke, C., Williams, B. J., and Xu, J.: A large and ubiquitous source of atmospheric formic acid, Atmos. Chem. Phys., 15, 6283-6304, 10.5194/acp-15-6283-2015, 2015.

van der Werf, G. R., Randerson, J. T., Giglio, L., van Leeuwen, T. T., Chen, Y., Rogers, B. M., Mu, M. Q., van Marle, M. J. E., Morton, D. C., Collatz, G. J., Yokelson, R. J., and Kasibhatla, P. S.: Global fire emissions estimates during 1997-2016, Earth Syst. Sci. Data, 9, 697-720, https://doi.org/10.5194/essd-9-697-2017, 2017.